2013-09-26

A New Catalyst-Embedded Hierarchical Air Electrode for High-Performance Li-O_2 Batteries

UTD AUTHOR(S): Xavier Lepró, Raquel Ovalle-Robles and Ray H. Baughman

Energy & Environmental Science

RSC Publishing

COMMUNICATION

View Article Online
View Journal | View Issue

A new catalyst-embedded hierarchical air electrode for high-performance Li–O_2 batteries†

Cite this: *Energy Environ. Sci.*, 2013, **6**, 3570

Received 5th June 2013
Accepted 25th September 2013

DOI: 10.1039/c3ee41910j

www.rsc.org/ees

Hee-Dae Lim,[a] Hyelynn Song,[b] Hyeokjo Gwon,[a] Kyu-Young Park,[a] Jinsoo Kim,[a] Youngjoon Bae,[a] Hyungsub Kim,[a] Sung-Kyun Jung,[a] Taewoo Kim,[b] Yong Hyup Kim,[bc] Xavier Lepró,[d] Raquel Ovalle-Robles,[d] Ray H. Baughman[d] and Kisuk Kang*[ae]

The Li–O_2 battery holds great promise as an ultra-high-energy-density device. However, its limited rechargeability and low energy efficiency remain key barriers to its practical application. Herein, we demonstrate that the ideal electrode morphology design combined with effective catalyst decoration can enhance the rechargeability of the Li–O_2 battery over 100 cycles with full discharge and charge. An aligned carbon structure with a hierarchical micro-nano-mesh ensures facile accessibility of reaction products and provides the optimal catalytic conditions for the Pt catalyst. The new electrode is highly reversible even at the extremely high current rate of 2 A g^{-1}. Moreover, we observed clearly distinct morphologies of discharge products when the catalyst is used. The effect of catalysts on the cycle stability is discussed.

Broader context

A great deal of interest has recently focused on Li–O_2 batteries as potential ultra-high-energy-density storage systems. The Li–O_2 battery can deliver the highest energy density among any other types of batteries because the lithium and oxygen directly react with each other in the absence of any heavy transition metals or crystal framework. However, during operation, the high energy density is rapidly lost because of poor rechargeability and low efficiency. Accordingly, recent research on Li–O_2 batteries has mainly focused on the enhancement of the cycle stability. In this work, we design a new air-electrode that incorporates catalysts in the hierarchically porous framework. The ideal catalyst-embedded air electrode could successfully retain the optimal air pathways and provide the condition for effective catalytic activity. The new electrode can deliver cycle performance over 100 cycles, with 1000 mA h g^{-1} at a high current rate of 2 A g^{-1}. Also, even with full discharge/charge, it could sustain its high energy up to 100 cycles. Additionally, we demonstrated how the Pt catalyst affected the morphology of the discharge products, which resulted in the enhanced cyclability of the Pt/CNT electrode.

Increasing demands for large-scale energy devices, such as electric vehicles (EVs) and hybrid electric vehicles (HEVs), require next-generation battery designs beyond those of the current Li-ion batteries (LIBs).[1–4] Among several candidates for post-LIBs, attention has focused on the Li–O_2 battery because of its remarkably high energy density, which can reach about 3500 W h kg^{-1}.[5–7] This high energy density is achievable because the electrochemical reaction between Li and O_2 in an Li–O_2 cell does not require a host crystal framework, which typically includes heavy transition metals such as redox elements.[8–10] Moreover, the availability of an unlimited source of oxygen from ambient air makes it more attractive as a next-generation battery. However, key limitations, such as poor cyclability and low coulombic efficiency, must be resolved for the Li–O_2 battery to be considered for extensive applications.

The major factors that affect the electrochemical performance of the Li–O_2 battery include the compatibility of the electrolyte, the electrode design, and the catalyst. At the early stages of Li–O_2 battery development, conventional LIB electrolytes, such as ethylene carbonate/dimethyl carbonate (EC/DMC) and propylene carbonate (PC), were used.[11–13] However, it was soon revealed that the carbonate-based electrolyte was unstable,

[a]*Department of Materials Science and Engineering, Research Institute of Advanced Materials, Seoul National University, 1 Gwanak-ro, Gwanak-gu, Seoul 151-742, Republic of Korea. E-mail: matlgen1@snu.ac.kr; Fax: +82 02 880 8197; Tel: +82 02 880 7088*

[b]*School of Mechanical and Aerospace Engineering, Seoul National University, 1 Gwanak-ro, Gwanak-gu, Seoul 151-742, Republic of Korea*

[c]*Institute of Advanced Aerospace Technology, Seoul National University, 1 Gwanak-ro, Gwanak-gu, Seoul 151-742, Republic of Korea*

[d]*Alan G. MacDiarmid NanoTech Institute, University of Texas at Dallas, Richardson, TX 75083-0688, USA*

[e]*Center for Nanoparticle Research, Institute for Basic Science, Seoul National University, Seoul 151-742, Republic of Korea*

† Electronic supplementary information (ESI) available: SEM and TEM images of the Pt/CNT electrode. TEM images of EDS line-mapping of the Pt/CNT electrode. XRD results of the as-prepared CNT and Pt/CNT electrodes. Electrochemical profiles of the Pt/CNT electrodes at different weight percentages of Pt. Time *vs.* voltage and current profiles of the Pt/CNT electrode over the first 10 cycles. Discharge/charge profiles of the Pt/CNT electrode between 2.0–4.5 V. GITT voltage profiles and XPS spectra of the Pt/CNT electrodes at each state. TEM images of the Pt/CNT electrode after the first discharge and charge. SEM images of the CNT electrode and the Pt/CNT electrode after the first discharge to 2.0 V and after cycling. Gas evolution result and FT-IR measurement of Pt/CNT electrodes. See DOI: 10.1039/c3ee41910j

yielding undesirable byproducts such as Li_2CO_3.[14,15] As an alternative, non-carbonate-based electrolytes, such as dimethoxyethane (DME) and tetraethylene glycol dimethylether (TEGDME), were suggested.[16–19] Although some improvements were achieved, they were also unstable and decomposed during prolonged cycling.[20] Accordingly, new reliable electrolytes for the Li–O_2 system remain elusive.[21,22] Also, the effect of salts and solvents for the Li–O_2 system needs to be further investigated.[22–24] While the electrolyte deterioration needs to be solved, the design of the air electrode is also an important factor that determines the capacity and the cycle efficiency.[25–27] Because the solid-state discharge products are deposited and decomposed on the air electrode, the transport of reactants and the distribution of catalysts in the electrode become critical in the recharging process. The use of porous graphene, nanoporous gold, and perovskite nanotubes for the air electrode clearly improved the electrochemical performance of the Li–O_2 cell.[28–31] More recently, we demonstrated that the optimal design of air pathways using hierarchical carbon nanotube (CNT) fibrils with controlled porosity can significantly enhance the cycle stability. The defect-less CNT fibrils could also minimize the formation of Li_2CO_3 byproduct similar to the nanoporous gold electrode.[31,32]

Here, we propose a new air-electrode design that incorporates catalysts in a hierarchically macroporous framework. A simple process of catalyst loading could successfully retain the optimal air pathways of the hierarchical carbon electrode and provide the right conditions for effective catalytic activity. The new electrode delivered stable cycle performance over 130 cycles with 1000 mA h g^{-1} at a high current rate of 2 A g^{-1}. Also, even with full discharge/charge, it could sustain high energy up to 100 cycles, which is very challenging for current Li–O_2 battery systems.

A sheet of aligned multiwalled nanotubes (MWNTs) was fabricated from a CNT forest, which was synthesized by catalytic chemical vapor deposition using acetylene gas as the source. The detailed procedures for the preparation of the CNT forest and the CNT fibrils are described in previous reports.[32,33] For the air electrode, 10 sheets of CNT fibrils were cross-woven layer-by-layer on a Ni mesh (Nillaco Corp., 12.7 mm in diameter), which was used as a current collector. No other conductive carbon source or binder was added. The prepared CNT electrode was coated with Pt nanoparticles by DC sputtering (BALTEC., SCD 005). The coating time and current were maintained at 100 s and 20 mA, respectively, and the weight percentage of Pt on the CNT is approximately 66%. The Li–O_2 cells were assembled in a Swagelok-type cell by stacking the prepared air-electrodes, a glass-fiber separator (Whatman GF/D, 2.7 μm pore size), and lithium metal in sequence. 1 M $LiPF_6$ in TEGDME electrolyte was used, and all the prepared cells were relaxed for 12 h in an oxygen atmosphere before testing. Electrochemical properties were measured using a potentio-galvanostat (WonA Tech, WBCS 3000, Korea). Each cell was carefully controlled and the outer pressure was maintained at oxygen atmosphere (770 Torr) using an automated throttle valve, which ensured high reproducibility and reliability. In all the experiments, the specific capacities were calculated based on the CNT weight, and the catalyst weight is not included. X-ray photoelectron spectroscopy (XPS, Thermo VG Scientific, Sigma Probe, UK) was used to analyze the reaction products at each step.

The air electrode was constructed based on hierarchically woven CNT fibrils with micro-mesh and nano-sized pores as shown in Fig. 1. The highly aligned CNT sheets were cross-woven such that they formed a mesh, which ensured a homogenous and well-ventilated structure. To make the catalyst-embedded air electrode, the CNT fibrils were loaded with Pt nanoparticles, which have been demonstrated to be an effective catalyst for the oxygen evolution reaction (OER).[34–39] Fig. 1b illustrates that all of the individual CNT strings were evenly coated with the nanoparticles. The CNTs were approximately 15 nm thick, and the size of the Pt particles was about 3–4 nm. The crosslinked CNT sheet with the open framework was maintained even after the deposition of the Pt nanoparticles, which assured that all of the CNT surfaces could be used as active reaction sites. The three-dimensionally aligned pore structure of the Pt–CNT fibrils not only allowed facile accessibility of Li ions and oxygen but also effectively exposed catalysts

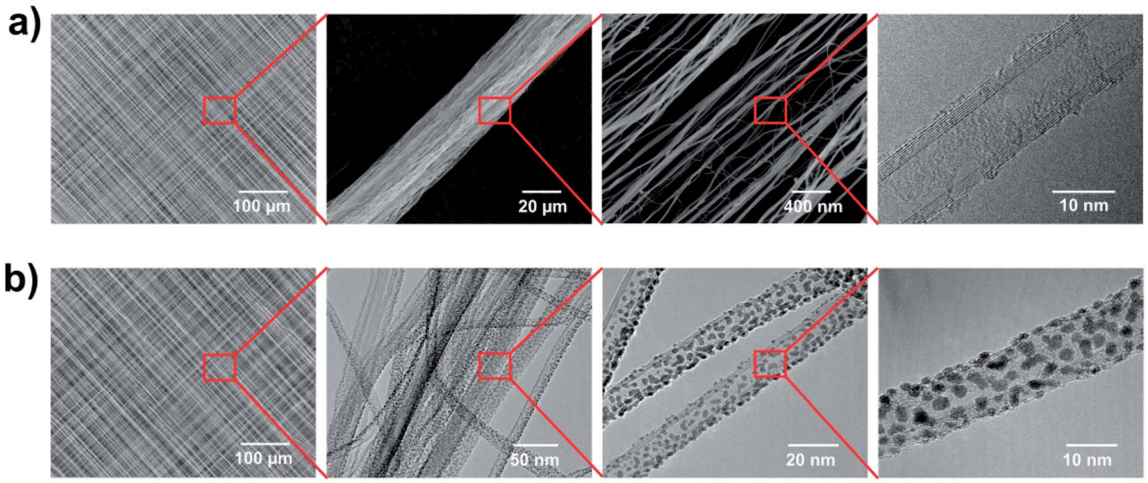

Fig. 1 (a) SEM images at various magnifications of the CNT electrode before Pt coating and a TEM image of a single CNT. (b) SEM and TEM images at various magnifications of the Pt/CNT electrode after Pt coating.

to the discharge products, thereby providing the ideal conditions for the catalytic reaction. Additional scanning electron microscopy (SEM) and transmission electron microscopy (TEM) images of the Pt-loaded CNT fibril electrode are given in the Supporting Information (Fig. S1–S3†). It is noteworthy that the highly aligned pore structure of the CNT sheets is advantageous in loading the nano-catalyst even in the inner space of the electrode. The open aligned structure could prevent preferential deposition on the outer side of the electrode even with the one-step physical deposition method. The simple physical deposition sustains the open electrode structure, while the wet-chemical deposition often causes difficulties in maintaining the initial structure because of the capillary forces during drying. The choice of catalyst and its loading weight are easily controllable, which will be beneficial for further studies of various catalysts.

The electrochemical performance of the Pt-loaded CNT fibril (Pt/CNT fibril) electrode was evaluated in comparison with that of a catalyst-free CNT fibril electrode. Fig. 2a shows the electrochemical profiles of the two electrodes at a current rate of 2000 mA g^{-1} with a depth of discharge of 1000 mA h g^{-1}. The Pt/CNT fibrils clearly reduced the overpotentials by about 500 mV during charge (OER). After multiple charge and discharge cycles, lower overpotentials, compared with the bare CNT fibril electrode, were maintained (Fig. S7†). The smaller overpotential was retained even at elevated current densities. Rate capability testing of the two electrodes (Fig. 2b) indicated that charging at 4000 mA g^{-1} still showed a lower overpotential by about 200–300 mV than that of the catalyst-free electrode, confirming the catalytic activity of Pt during OER. While the polarization still increased with the higher current density, the overpotential of the Pt/CNT electrode remained considerably lower. However, it should be noted that the OER activity of the Pt catalyst was particularly notable at a low depth of discharge (about 1000 mA h g^{-1}). If we consider the deep discharge state to 2.0 V (about 2500 mA h g^{-1}), the OER overpotential was not significantly reduced during the recharge even when the same catalyst was used (Fig. S8†). Because the insulating discharge products were deposited on the electrode surface, the active surface area was gradually passivated by the discharge products. In the deep discharge state, a large amount of discharge products would form a thick insulating film layer and significantly passivate the catalytic activity in terms of decomposing the products. Therefore, the catalytic activity in this case would not be as dramatic as for a low depth of discharge. Thus, in Li–O_2 batteries, the relationship between the catalyst activity and the depth of discharge must be considered.

The cycle stability of the Pt/CNT fibril electrode was evaluated (Fig. 3). Remarkably stable cycles were achieved for capacity-limited cycling at 1000 mA h g^{-1}, which could continue over 130 cycles (Fig. 3a). This is far superior to the bare CNT fibril electrode (the inset of Fig. 3a), which was stable only up to 70 cycles under the same conditions. The enhanced cycling performance of the Pt/CNT electrode was observed even in the

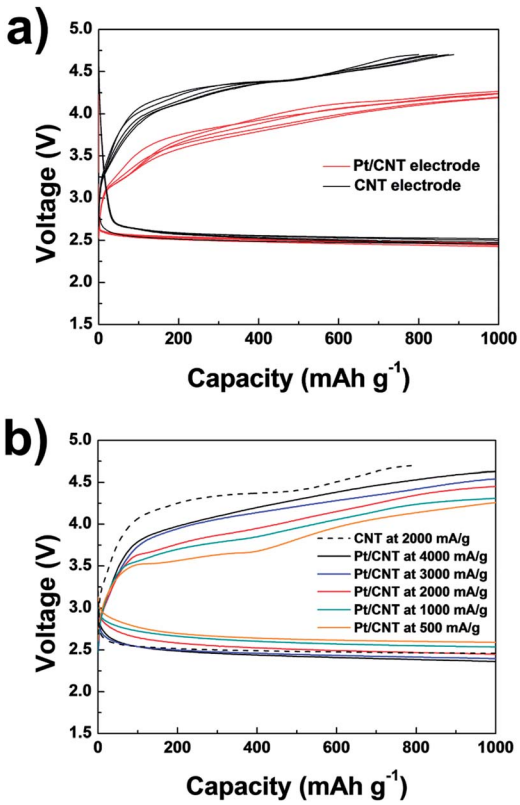

Fig. 2 (a) Electrochemical profiles of the CNT (black line) and Pt/CNT (red line) electrodes at a current rate of 2000 mA g^{-1} with the limited depth of discharge at 1000 mA h g^{-1}. (b) Rate capabilities of the Pt/CNT electrode.

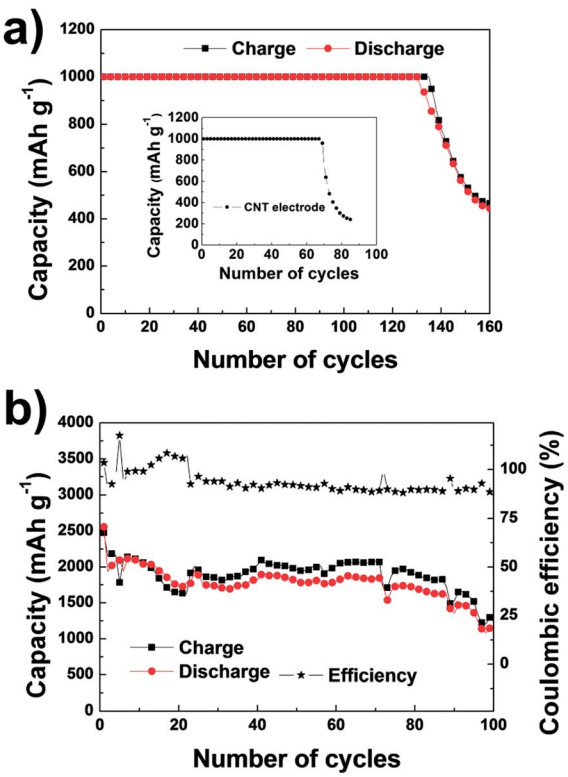

Fig. 3 Cyclability of the Li–O_2 cell with a Pt/CNT electrode at a current rate of 2000 mA g^{-1} with (a) the limited depth of discharge at 1000 mA h g^{-1} and (b) fully discharged/charged between 2.0 and 4.7 V (inset: cyclability of the Li–O_2 cell with a CNT electrode).

full discharge/charge cycle protocols between 2.0 and 4.7 V (Fig. 3b). Compared with the bare CNT fibril electrode, which could achieve only about 30 full discharge/charge cycles,[32] the Pt/CNT electrode had an outstanding capability for reversible formation and decomposition of Li_2O_2 with high efficiency. More than 100 cycles of full discharge/charge have rarely been achieved by Li–O_2 batteries because of clogging of the discharge products and incomplete decomposition reactions during prolonged cycling. Although the low loading weight of CNT sheets with an open framework is an obvious drawback for practical applications, the high reversibility of the Pt/CNT electrode even during prolonged cycling at high rates is certainly notable. It is also interesting to note that the enhanced cycle stability was achieved for full discharge/charge, even though the reduction of the overpotential under the same conditions was not remarkable. This discrepancy will be discussed later with respect to the nature of the deposition of the discharge products.

To elucidate the origin of the enhanced cycle stability, the morphological changes in the discharge products during the discharge and charge were investigated by tracing the electron microscopy images at different DODs (depths of discharge) of the electrode. Fig. 4(a–d) show TEM and SEM images after the first discharge at DODs of 1000 mA h g^{-1} and 2500 mA h g^{-1}. After the first discharge at 1000 mA h g^{-1} (Fig. 4a and b), uniform formation of discharge products was found on the CNT surfaces. Amorphous-like discharge products with a few nanometers thick, which were confirmed to be Li_2O_2 and a small amount of Li_2CO_3 (XPS, Fig. S9†), grew continuously on the CNT surfaces. Li_2CO_3 might be generated from the electrolyte decomposition.[40–42] Because of the uniform growth of the discharge products, the open framework of the parent CNT sheets was well maintained without clogging (Fig. 4 and S11†). This demonstrated the high durability of the Pt/CNT electrode. With deep discharge, the thickness of the discharge products continuously increased with continuous and uniform formation on the CNT surfaces (Fig. 4c and d). Also, the formed discharge products were clearly decomposed after charging (Fig. S12†). This was in good agreement with the XPS (Fig. S9†), *ex-situ* FT-IR (Fig. S13†) and galvanostatic intermittent titration technique (GITT, Fig. S14†) data that proved the high reversibility of the Pt/CNT electrode. Although the initial cycles show a great reversibility, Li_2CO_3 from the electrolyte decomposition gradually increases as cycle goes on and wholly covers the active CNT surface at the point of cycle failure (Fig. S15†).

Interestingly, we found that the Pt catalyst strongly affected the morphologies of the discharge products. While the bare CNT fibril electrode yielded large beads about 80 nm in size after discharge (Fig. 4e and f), such beads were not seen on the Pt/CNT electrode. Instead, simply a thicker discharge product was formed. The additional SEM images at various magnifications (Fig. S16†) demonstrate the differences between the bare CNT and the Pt/CNT electrodes more clearly. It was previously shown that the formation of numerous large beads accompanies cycle degradation.[32] As the numbers of beads substantially increased with cycling, the beads completely covered the active CNT surfaces by the end of cycling, resulting in cycle failure in the case of the bare CNT electrode (Fig. S17†). Segregation of the discharge products in the form of beads can

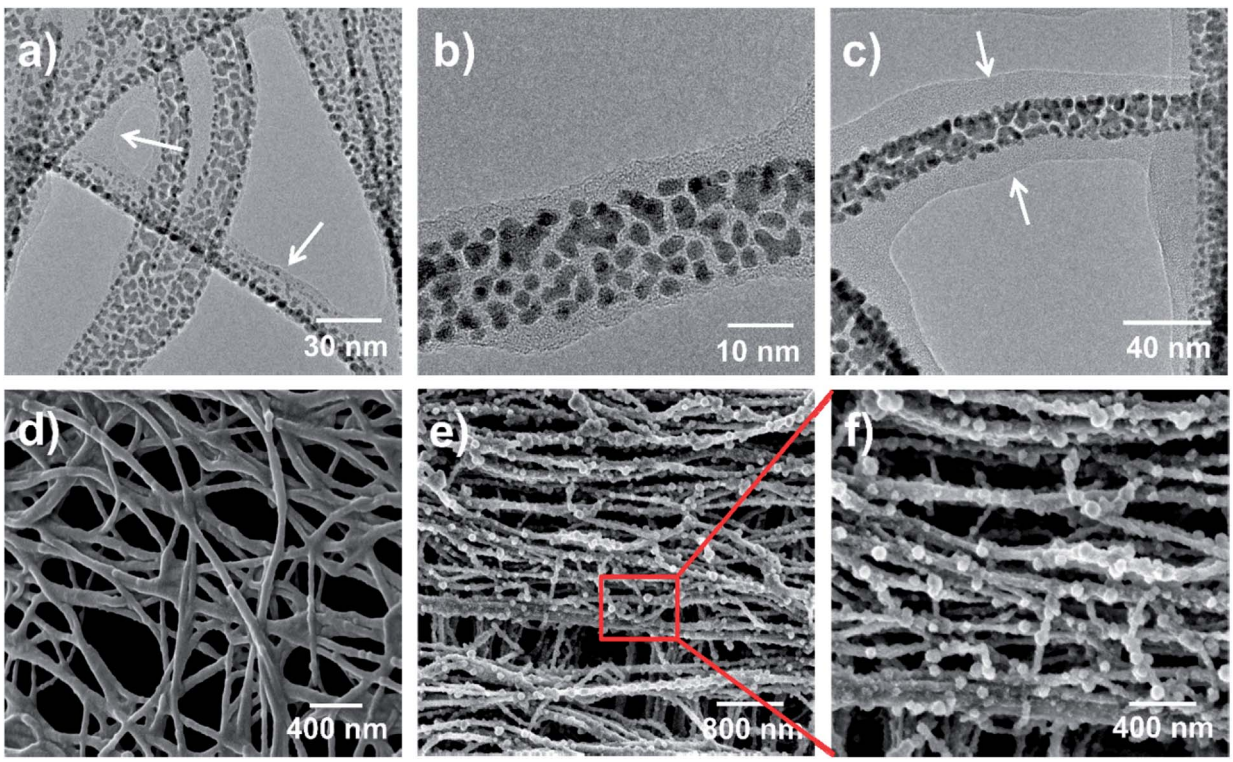

Fig. 4 (a and b) TEM images of the Pt/CNT electrode after the first discharge at 1000 mA h g^{-1}. (c) TEM and (d) SEM images of the Pt/CNT electrode after full discharge to 2.0 V. (e and f) SEM images of the catalyst-free CNT electrode after discharge.

lead to electrical isolation, which can limit recharging (decomposition) upon cycling and ultimately lead to failure. With the Pt/CNT electrode, in contrast, the uniform deposition of products on the surfaces continued without the formation of large beads even at the deep discharge states (Fig. 4 and S16†). We believe that the uniformly distributed nano-catalyst promotes the homogeneous film-like formation of the discharge products. Furthermore, the absence of isolated discharge products in the form of beads could prevent the loss of active materials. This implies that the OER-enhancing Pt catalyst not only helped to reduce the charging polarization but also controlled the morphology of the discharge products, thereby contributing to the enhanced cycle stability. It is worthwhile to note that despite the insignificant reduction of overpotential with deep discharge/charge cycling, the Pt-embedded electrode maintained its higher cycle stability. This behavior is attributed to the dual roles of the Pt OER catalyst, *i.e.*, promoting uniform deposition of the discharge products even for deep discharge states and facilitating the decomposition reaction upon re-charging.

The hierarchically porous air electrode incorporating a catalyst was designed by cross-weaving aligned CNT sheets and embedding Pt nanoparticles. The ideal catalyst-embedded air electrode contributed to the facile accessibility of lithium and oxygen and provided the conditions for effective catalytic activity. The remarkable cycle stability over 100 cycles with full discharge/charge could be achieved at the high current rate of 2 A g^{-1}; this is also attributed to the dual function of the embedded Pt catalyst, which not only reduced the charge polarization substantially, but also promoted the homogeneous film-like formation of the discharge products. The design of an air electrode that considers both the transport pathway and the catalyst distribution is expected to guide further Li–O_2 battery development.

Acknowledgements

This work was supported by the Human Resources Development program (20124010203320) of the Korea Institute of Energy Technology Evaluation and Planning (KETEP) grant funded by the Korea government Ministry of Trade, Industry and Energy and supported by a National Research Foundation of Korea Grant funded by the Korean Government (MEST) (NRF-2009-0094219). This work was supported by the Research Center Program of IBS (Institute for Basic Science) in Korea. This work was also supported by the National Research Foundation of Korea (Grant No.2013-000688) and the National Research Foundation of Korea (Grant No.2013-50 000688, 2013-042193).

Notes and references

1 F. Cheng and J. Chen, *Nat. Chem.*, 2012, **4**, 962–963.
2 P. Hartmann, C. L. Bender, M. Vračar, A. K. Dürr, A. Garsuch, J. Janek and P. Adelhelm, *Nat. Mater.*, 2012, **12**, 228–232.
3 H.-G. Jung, J. Hassoun, J.-B. Park, Y.-K. Sun and B. Scrosati, *Nat. Chem.*, 2012, **4**, 579–585.
4 J.-S. Lee, S. Tai Kim, R. Cao, N.-S. Choi, M. Liu, K. T. Lee and J. Cho, *Adv. Energy Mater.*, 2011, **1**, 34–50.
5 P. G. Bruce, S. A. Freunberger, L. J. Hardwick and J.-M. Tarascon, *Nat. Mater.*, 2012, **11**, 19–29.
6 R. Black, S. H. Oh, J.-H. Lee, T. Yim, B. Adams and L. F. Nazar, *J. Am. Chem. Soc.*, 2012, **134**, 2902–2905.
7 Y. Cui, Z. Wen, X. Liang, Y. Lu, J. Jin, M. Wu and X. Wu, *Energy Environ. Sci.*, 2012, **5**, 7893–7897.
8 Z. Peng, S. A. Freunberger, L. J. Hardwick, Y. Chen, V. Giordani, F. Bardé, P. Novák, D. Graham, J.-M. Tarascon and P. G. Bruce, *Angew. Chem.*, 2011, **123**, 6475–6479.
9 A. Kraytsberg and Y. Ein-Eli, *J. Power Sources*, 2011, **196**, 886–893.
10 J. Christensen, P. Albertus, R. S. Sanchez-Carrera, T. Lohmann, B. Kozinsky, R. Liedtke, J. Ahmed and A. Kojic, *J. Electrochem. Soc.*, 2012, **159**, R1–R30.
11 J. Read, *J. Electrochem. Soc.*, 2002, **149**, A1190–A1195.
12 A. Débart, A. J. Paterson, J. Bao and P. G. Bruce, *Angew. Chem.*, 2008, **120**, 4597–4600.
13 S. D. Beattie, D. M. Manolescu and S. L. Blair, *J. Electrochem. Soc.*, 2009, **156**, A44–A47.
14 S. A. Freunberger, Y. Chen, Z. Peng, J. M. Griffin, L. J. Hardwick, F. Bardé, P. Novák and P. G. Bruce, *J. Am. Chem. Soc.*, 2011, **133**, 8040–8047.
15 Z. Zhang, J. Lu, R. S. Assary, P. Du, H. H. Wang, Y. K. Sun, Y. Qin, K. C. Lau, J. Greeley, P. C. Redfern, H. Iddir, L. A. Curtiss and K. Amine, *J. Phys. Chem. C*, 2011, **115**, 25535–25542.
16 B. D. McCloskey, D. S. Bethune, R. M. Shelby, G. Girishkumar and A. C. Luntz, *J. Phys. Chem. Lett.*, 2011, **2**, 1161–1166.
17 C. O. Laoire, S. Mukerjee, E. J. Plichta, M. A. Hendrickson and K. M. Abraham, *J. Electrochem. Soc.*, 2011, **158**, A302–A308.
18 F. Li, T. Zhang, Y. Yamada, A. Yamada and H. Zhou, *Adv. Energy Mater.*, 2013, **3**, 532–538.
19 C. S. Park, K. S. Kim and Y. J. Park, *J. Power Sources*, 2013, **244**, 72–79.
20 S. A. Freunberger, Y. Chen, N. E. Drewett, L. J. Hardwick, F. Bardé and P. G. Bruce, *Angew. Chem., Int. Ed.*, 2011, **50**, 8609–8613.
21 W. Walker, V. Giordani, J. Uddin, V. S. Bryantsev, G. V. Chase and D. Addison, *J. Am. Chem. Soc.*, 2013, **135**, 2076–2079.
22 E. Nasybulin, W. Xu, M. H. Engelhard, Z. Nie, S. D. Burton, L. Cosimbescu, M. E. Gross and J.-G. Zhang, *J. Phys. Chem. C*, 2013, **117**, 2635–2645.
23 P. Du, J. Lu, K. C. Lau, X. Luo, J. Bareno, X. Zhang, Y. Ren, Z. Zhang, L. A. Curtiss, Y.-K. Sun and K. Amine, *Phys. Chem. Chem. Phys.*, 2013, **15**, 5572–5581.
24 L. Suo, Y.-S. Hu, H. Li, M. Armand and L. Chen, *Nat. Commun.*, 2013, **4**, 1481.
25 X. Lin, L. Zhou, T. Huang and A. Yu, *J. Mater. Chem. A*, 2013, **1**, 1239–1245.
26 V. Etacheri, D. Sharon, A. Garsuch, M. Afri, A. A. Frimer and D. Aurbach, *J. Mater. Chem. A*, 2013, **1**, 5021–5030.
27 M. Mirzaeian and P. J. Hall, *Electrochim. Acta*, 2009, **54**, 7444–7451.

28 J. Xiao, D. Mei, X. Li, W. Xu, D. Wang, G. L. Graff, W. D. Bennett, Z. Nie, L. V. Saraf, I. A. Aksay, J. Liu and J.-G. Zhang, *Nano Lett.*, 2011, **11**, 5071–5078.
29 J.-J. Xu, D. Xu, Z.-L. Wang, H.-G. Wang, L.-L. Zhang and X.-B. Zhang, *Angew. Chem., Int. Ed.*, 2013, **52**, 3887–3890.
30 R. R. Mitchell, B. M. Gallant, C. V. Thompson and Y. Shao-Horn, *Energy Environ. Sci.*, 2011, **4**, 2952–2958.
31 Z. Peng, S. A. Freunberger, Y. Chen and P. G. Bruce, *Science*, 2012, **337**, 563–566.
32 H.-D. Lim, K.-Y. Park, H. Song, E. Y. Jang, H. Gwon, J. Kim, Y. H. Kim, M. D. Lima, R. O. Robles, X. Lepró, R. H. Baughman and K. Kang, *Adv. Mater.*, 2013, **25**, 1348–1352.
33 M. Zhang, S. Fang, A. A. Zakhidov, S. B. Lee, A. E. Aliev, C. D. Williams, K. R. Atkinson and R. H. Baughman, *Science*, 2005, **309**, 1215–1219.
34 S. Meini, N. Tsiouvaras, K. U. Schwenke, M. Piana, H. Beyer, L. Lange and H. A. Gasteiger, *Phys. Chem. Chem. Phys.*, 2013, **15**, 11478–11493.
35 J. R. Harding, Y.-C. Lu, Y. Tsukada and Y. Shao-Horn, *Phys. Chem. Chem. Phys.*, 2012, **14**, 10540–10546.
36 Y. Lu, Z. Wen, J. Jin, Y. Cui, M. Wu and S. Sun, *J. Solid State Electrochem.*, 2012, **16**, 1863–1868.
37 F.-S. Ke, B. C. Solomon, S.-G. Ma and X.-D. Zhou, *Electrochim. Acta*, 2012, **85**, 444–449.
38 L. Wang, M. Ara, K. Wadumesthrige, S. Salley and K. Y. S. Ng, *J. Power Sources*, 2013, **234**, 8–15.
39 E. Yoo and H. Zhou, *ACS Nano*, 2011, **5**, 3020–3026.
40 B. D. McCloskey, R. Scheffler, A. Speidel, D. S. Bethune, R. M. Shelby and A. C. Luntz, *J. Am. Chem. Soc.*, 2011, **133**, 18038–18041.
41 C. J. Barile and A. A. Gewirth, *J. Electrochem. Soc.*, 2013, **160**, A549–A552.
42 J. R. Harding, Y.-C. Lu, Y. Tsukada and Y. Shao-Horn, *Phys. Chem. Chem. Phys.*, 2012, **14**, 10540–10546.

Supporting Information

A New Catalyst-embedded Hierarchical Air Electrode for High-performance Li−O_2 Batteries

Hee-Dae Lim,[a] *Hyelynn Song,*[b] *Hyeokjo Gwon,*[a] *Kyu-Young Park,*[a] *Jinsoo Kim,*[a] *Youngjoon Bae,*[a] *Hyungsub Kim,*[a] *Sung-Kyun Jung,*[a] *Taewoo Kim,*[b] *Yong Hyup Kim,*[bc] *Xavier Lepró,*[d] *Raquel Ovalle-Robles,*[d] *Ray H. Baughman*[d] *and Kisuk Kang*[*ae]

* Corresponding author, matlgen1@snu.ac.kr

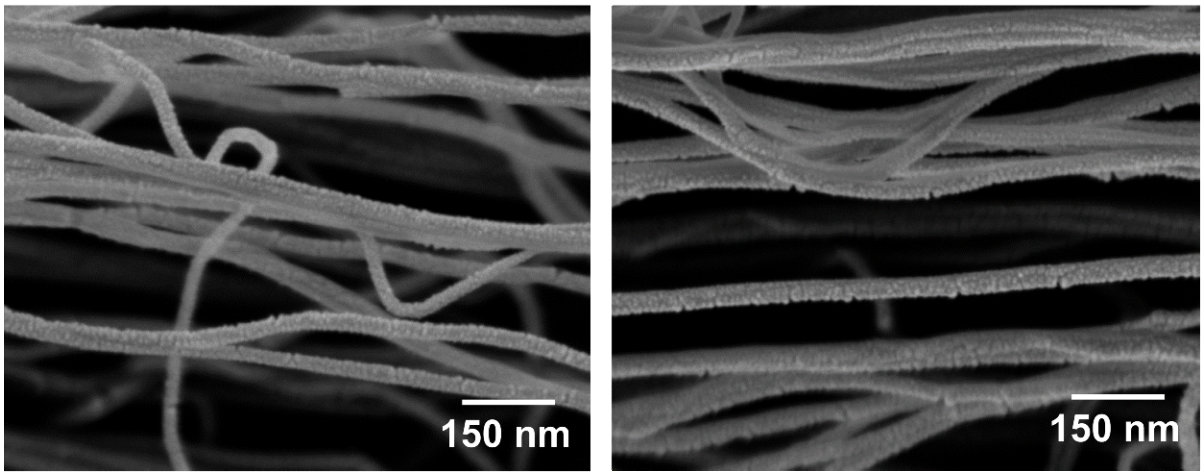

Figure S1. SEM images of the Pt/CNT electrode. The scabrous surface texture indicates that all of the individual CNT strings are homogenously coated with Pt nanoparticles.

.

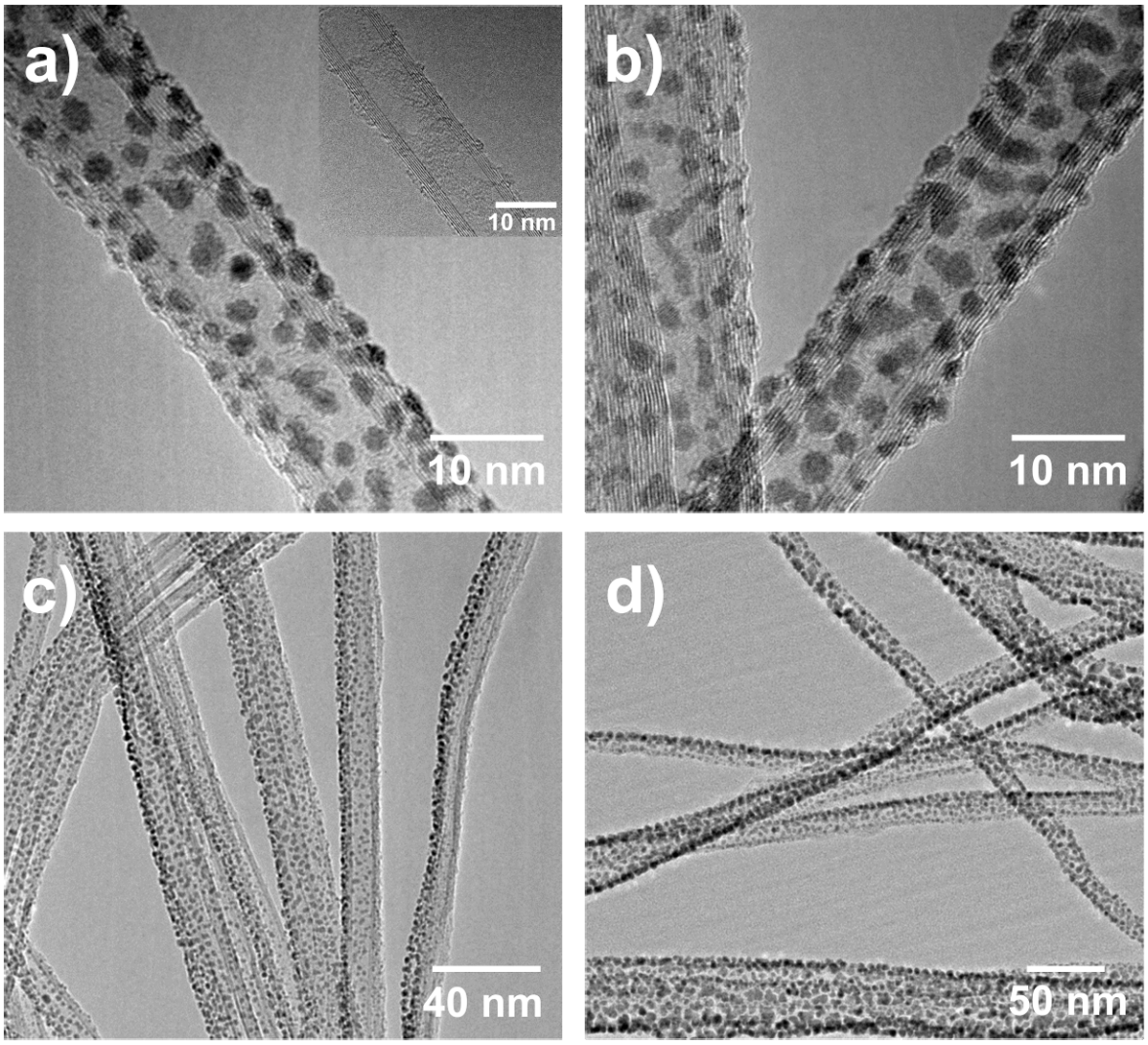

Figure S2. Additional TEM images of the Pt/CNT electrode at various magnifications (Inset: TEM image of the as-prepared CNT).

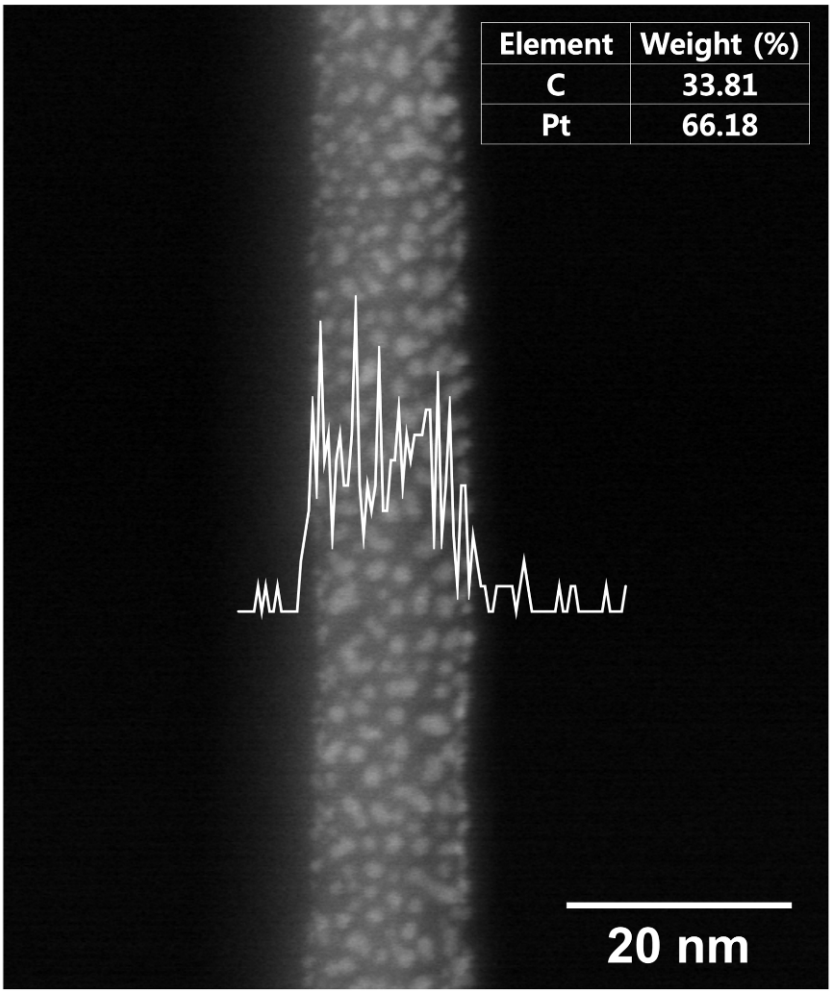

Figure S3. TEM image of a single string of Pt/CNT at a high magnification and the EDS line map of Pt. The inset table shows the quantitative analysis of Pt and C.

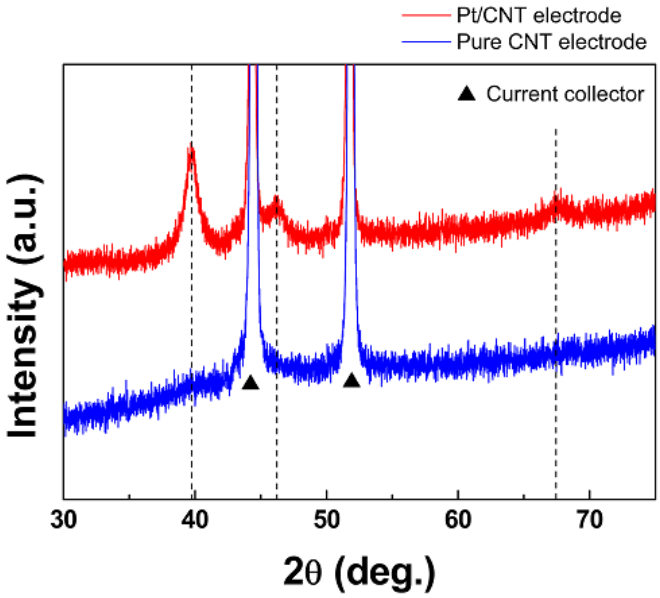

Figure S4. XRD results of the as-prepared CNT and Pt/CNT electrodes. The dash line corresponds to Pt.

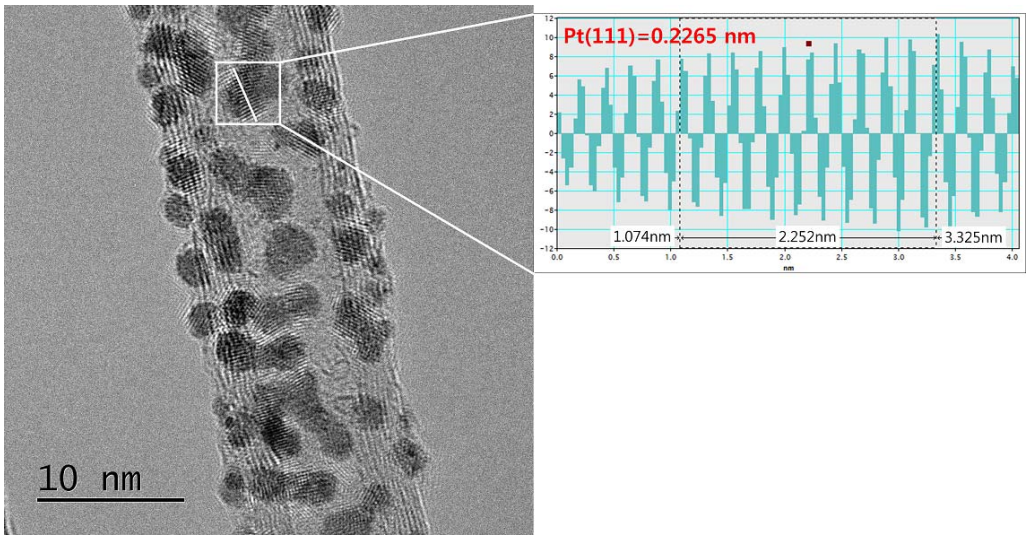

Figure S5. HR-TEM image of Pt/CNT and the d-spacing of the incorporated particle. The figure shows the average intervals of the incorporated particle (white line) is about 0.2252nm, which agrees well with the d-spacing between two adjacent lattice fringes of Pt (111) plane.

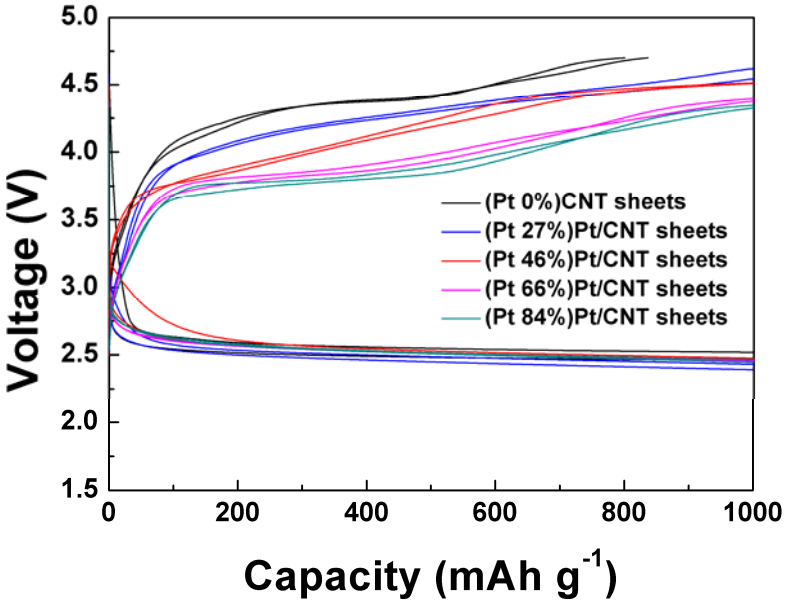

Figure S6. Electrochemical profiles of the PT/CNT electrodes at a current rate of 2,000 mA g^{-1} with the limited depth of discharge at 1000 mAh g^{-1} at different weight percentages of Pt. As the weight percentages of Pt increase, the polarization is gradually decreased. However, it should be noted that the catalytic activity of Pt is not obviously increased over 66 %.

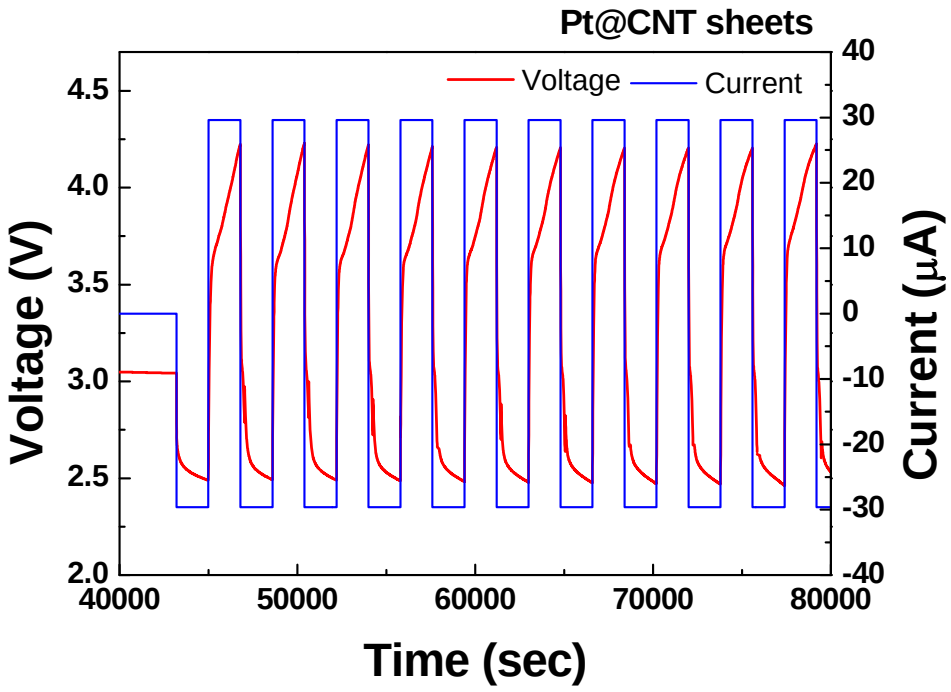

Figure S7. Time *vs.* voltage and current profiles of the first 10 cycles for the Pt/CNT electrode. Before the test, all of the cells were relaxed in an oxygen atmosphere for 12 h.

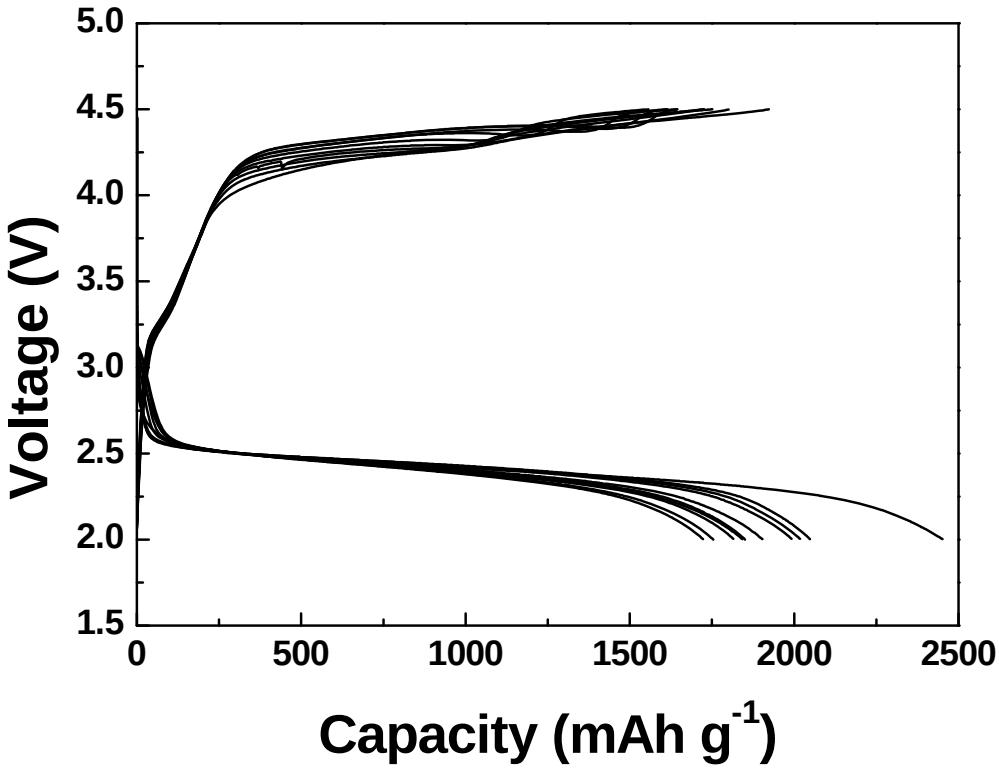

Figure S8. Discharge/charge profiles of the Pt/CNT electrode at 2000 mA g^{-1} with full discharge/charge between 2.0–4.5 V.

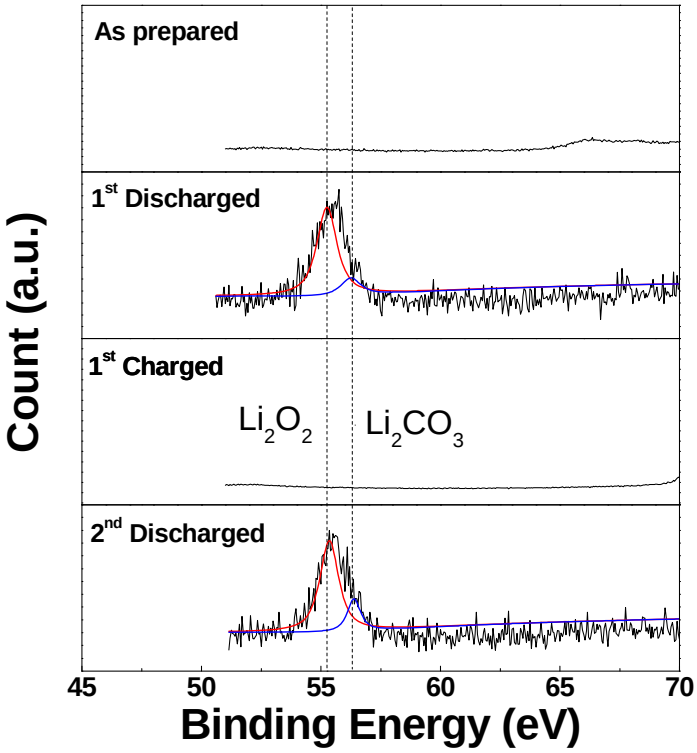

Figure S9. XPS spectra of Li 1s for the Pt/CNT electrode at each state. In the initial cycles, the major reaction product was Li_2O_2, while a small amount of Li_2CO_3 was also present.

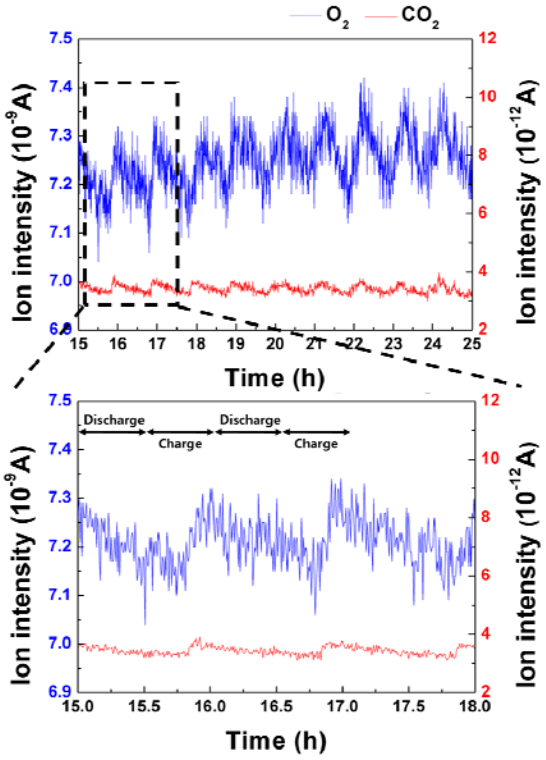

Figure S10. Gas (O_2 and CO_2) evolution results of the PT/CNT electrodes measured by DEMS. Each discharge and charge time is 30 minute.

Differential electrochemical mass spectrometry (DEMS) was carried out to investigate the gas consumption/evolution results. DEMS consists of a combination of a mass spectrometer (MS) (HPR-20, Hiden Analytical) and a potentio-galvanostat (WonA Tech, WBCS 3000, Korea). The gases that evolved during the discharge/charge process were swept into a MS upon the start of the electrochemical test. The flow rate of carrier gas (oxygen) swept into the MS is 0.5 cc/min.

During the discharge, the ion intensity of oxygen gradually decrease, which implies that the oxygen is used for the formation of discharge products. Almost same amount of oxygen is evolved during the charge implying the reversibility of the reaction. The theoretical volume of evolved/ consumed oxygen ($2Li^+ + O_2 + 2e^- \rightarrow Li_2O_2$) is 0.01458 mL for the one cycle in

our system. The average volume of the used oxygen is 0.01425 mL, which is well matched with the theoretical value. Also the average volume of CO_2 gas evolved during charge is only 5.2 % (0.00075 mL) compared to that of oxygen. Relatively small amount of CO_2 is evolved during charge. The detection of CO_2 gas means the existence of lithium carbonate, which is well corresponds to XPS, FT-IR and TEM in the manuscript. Small amount of lithium carbonate inevitably exist in the current Li-air batteries using carbon substrate and TEGDME electrolyte. It is partly decomposed during charge, however, some remains and gradually stacked during cycles, which deteriorates the cycle life of Li air cells.

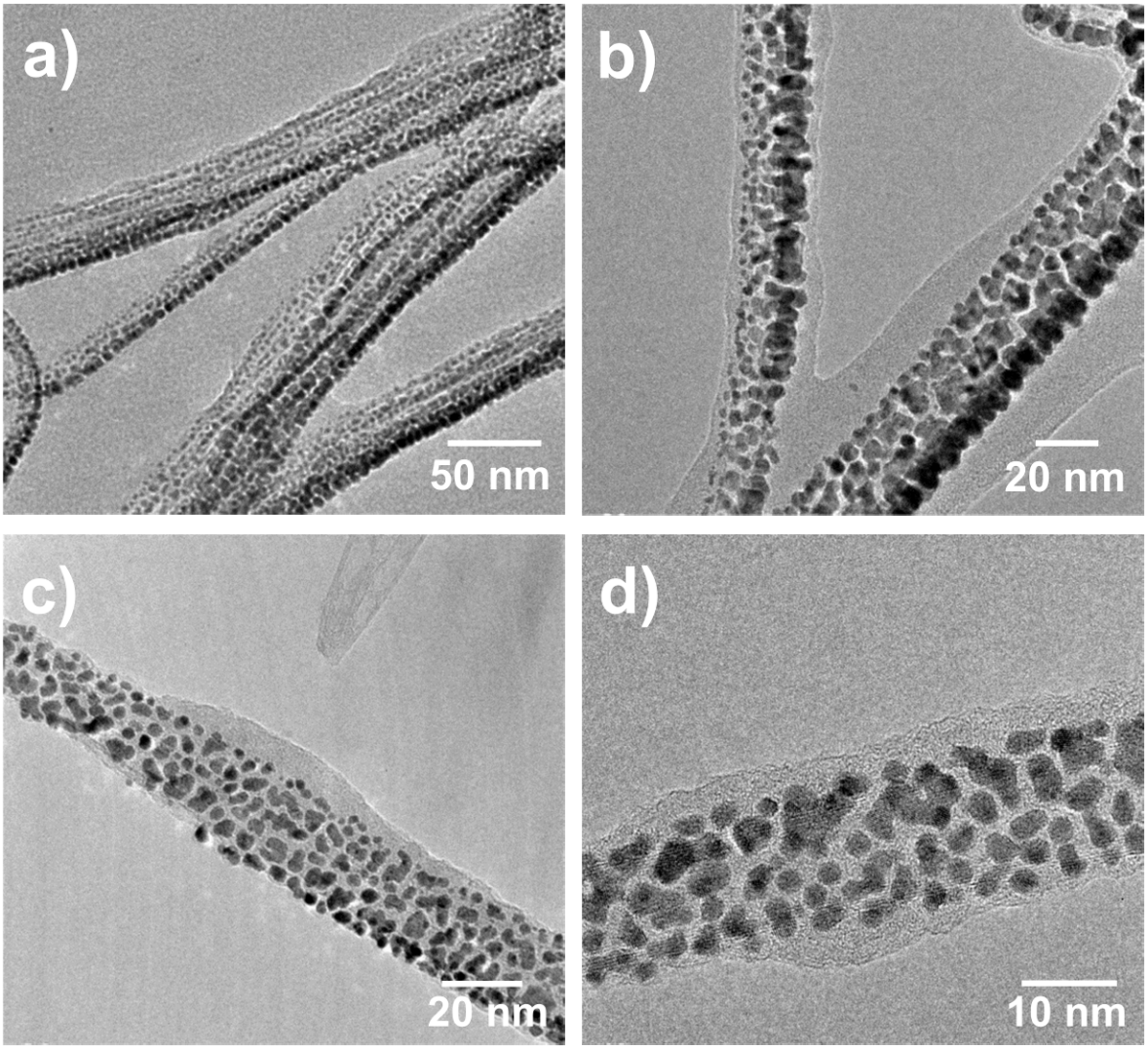

Figure S11. Various TEM images of the Pt/CNT electrode after the initial discharge to 1,000 mAh g^{-1}.

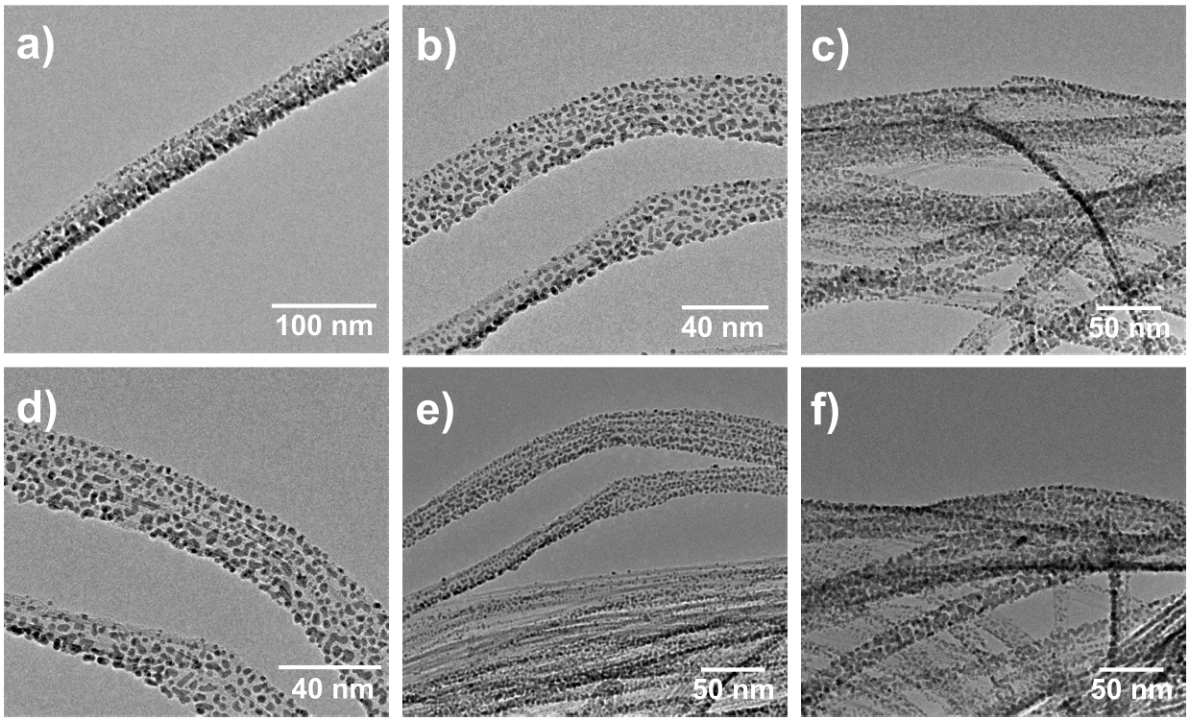

Figure S12. Various TEM images of the Pt/CNT electrode after the first charge. The discharge products were clearly decomposed and clean CNT surfaces were observed.

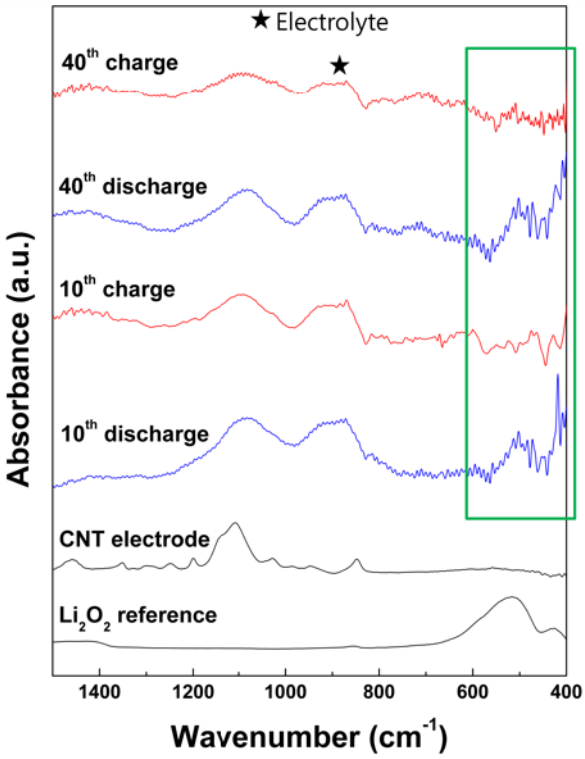

Figure S13. FT-IR measurement of air electrodes collected at 10th and 40th discharge/charge.

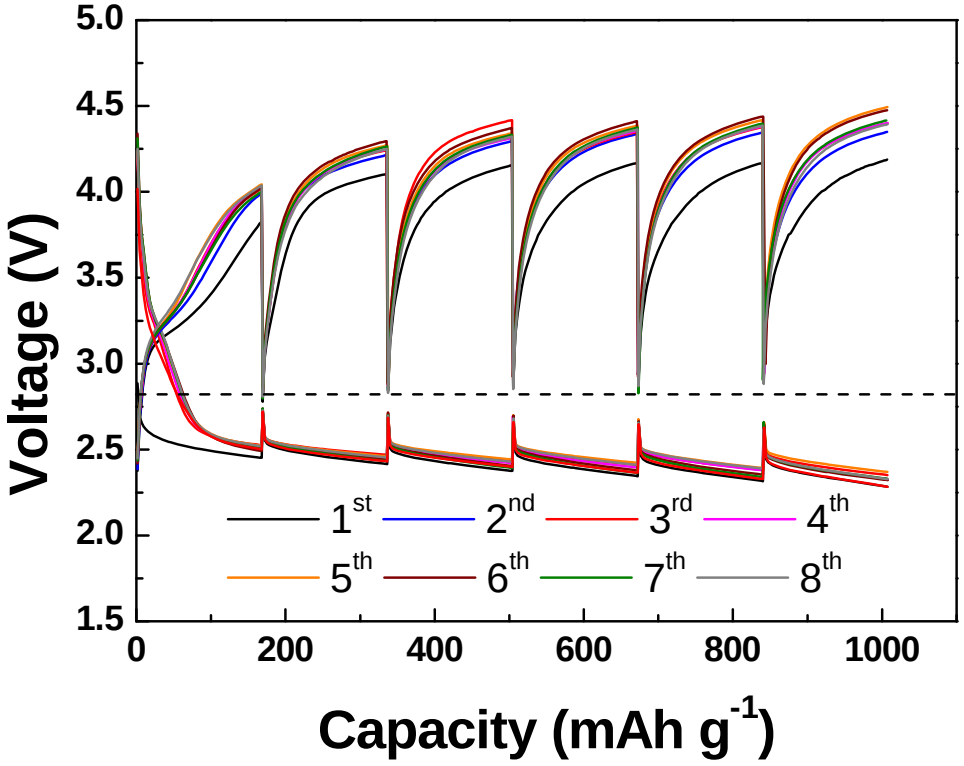

Figure S14. (a) GITT voltage profiles of the Pt/CNT electrode. During discharge/charge, the relaxation potential at each step approached the theoretical formation potential of Li_2O_2 (2.96 V).

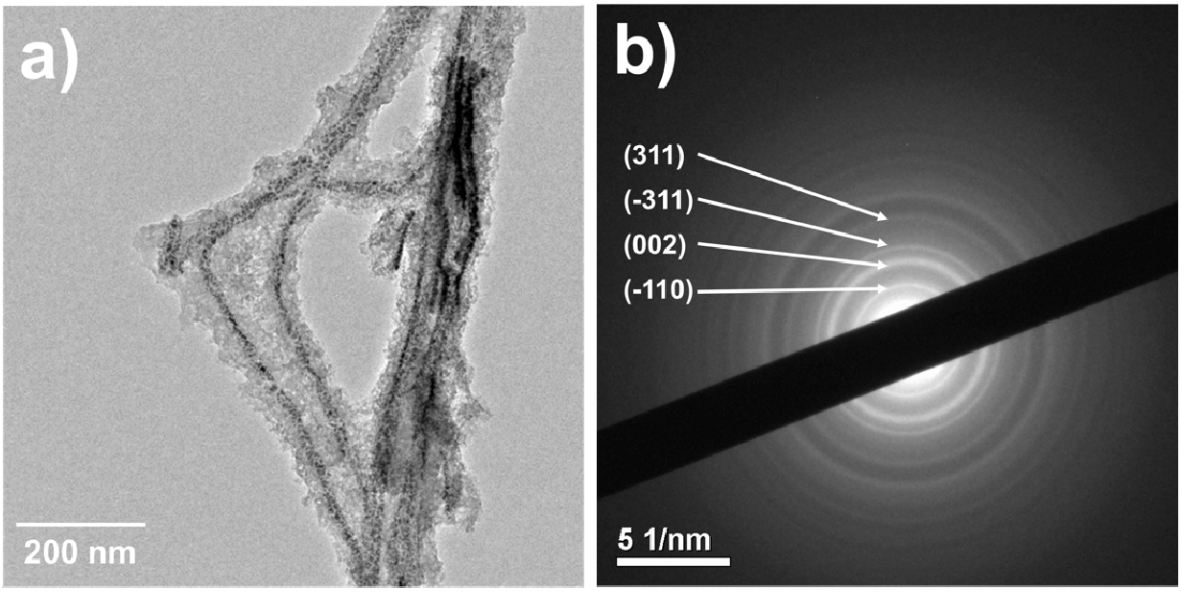

Figure S15. (a) TEM image of the Pt/CNT electrode at the end of cycles. (b) The corresponding diffraction pattern proves the formation of Li_2CO_3 at the surface of Pt/CNT electrode.

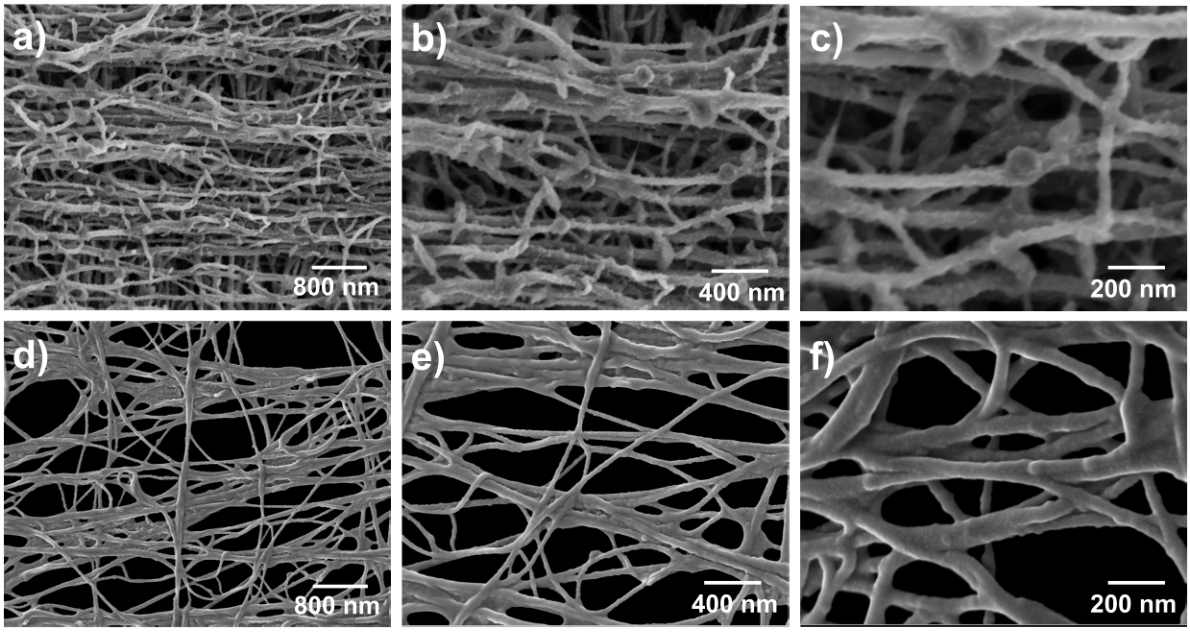

Figure S16. SEM images at various magnifications of (a–c) the CNT electrode without catalyst and (d–f) the Pt/CNT electrode after the first discharge to 2.0 V.

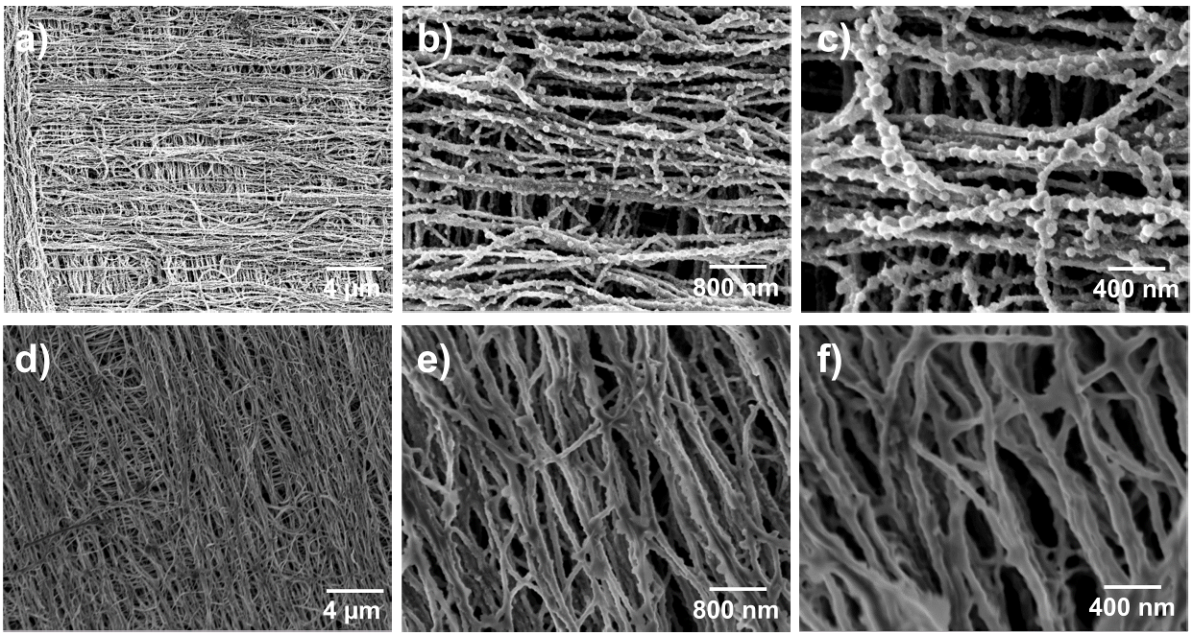

Figure S17. SEM images at various magnifications of (a–c) the CNT electrode without catalyst and (d–f) the Pt/CNT electrode at the end of cycles (30 and 100 cycles, respectively).